Géotechnique
Article In Press
Acceptation date : December 2024
https://doi.org/10.1680/jgeot.24.01097
https://archimer.ifremer.fr/doc/00926/103745/

Particle crushability's role in liquefaction: insights from Mayotte submarine slopes

Terzariol Marco [1,*], Sultan Nabil [1], Garziglia Sebastien [1], Jorry Stephan [1], Jouet Gwenael [1]

[1] Geo-Ocean UMR6538, IFREMER, CNRS, UBO, UBS, 29280 Plouzane, France

* Corresponding author : Marco Terzariol, email address : marco.terzariol@ifremer.fr

Abstract :

Since 10 May, 2018, a significant number of volcanic and seismic events have been recorded in Mayotte, in the Comoros Archipelago of the Indian Ocean. Detailed bathymetry of Mayotte′s eastern regions has uncovered steep underwater slopes. A recent study in the area investigated liquefaction-prone layers associated with low sea-level depositions. However, the reason for the presence of such 'weak zones' remained unknown. In the present study, we examined samples from Mayotte's slopes to investigate the reason for liquefaction at the particle-scale of such layers. Our results show that biogenic particles in naturally sedimented environments can crush under cyclic or static loading even with large amounts of fines. In the case of Mayotte's slopes, the external loading threshold was found to be 500 kPa under K0-conditions. Our findings highlight the complex behavior of biogenic-dominant sediments, their impact on classification and overall behavior, and their potential implications for the design of wind farms.

Keywords : particle crushing/crushability, liquefaction, calcareous soil

Introduction

Since 10 May 2018, Mayotte (Comoros archipelago, Indian Ocean) has experienced significant volcanic and seismic activity with more than 11,000 earthquakes (magnitude > 5.9) and a seafloor deformation of up to 200 mm/yr. These events formed a volcanic edifice named Fani Maore, >800 m in height and 5 km^3, which has not ceased to deform since its identification. It is considered the largest active submarine eruption ever documented (Cesca et al. 2020; Feuillet et al. 2021). Bathymetry maps of the eastern area of Mayotte's island show steep submarine slopes locally exceeding 35° (Rinnert et al. 2021) which, in a high seismicity scenario, can become vulnerable to ground shaking and eventually generate tsunamis (Audru et al. 2006; Poulain et al., 2022). Submarine sediments offshore Mayotte consist of carbonate and hemipelagic particles from barrier-reef production, as well as volcanic-derived grains from continental and volcanic erosion. During high sea-level periods (when the barrier was flooded), aragonite and high-magnesium calcite dominated the depositional behaviour; whilst at lowstand, planktic-origin low-magnesium calcite accumulates, which translates into fluctuations in γ-density and magnetic susceptibility MS measured on sediment cores obtained in this area (Sultan et al. 2023; Rinnert et al. 2021). Liquefaction-prone layers (classified as 'weak zones' with low MS and γ-density) were correlated to periods of low sea level and low-magnesium calcite content (Sultan et al. 2023). However, the underlying factor increasing the susceptibility of such layers to liquefaction is unknown.

Liquefaction is classically defined as the loss of strength in saturated, cohesionless soils due to increased pore-water pressure subjected to an external load. A rise in the amount of fine particles within a sandy matrix is likely to enhance resistance to liquefaction (Ishihara 1993; Youd 1998; Boulanger and Idriss 2004; Bray and Sancio 2006; Park and Kim 2013; Marto et al. 2015; Ghani and Kumari, 2020). This criterion can be anticipated in the evaluation of indirect liquefaction-susceptibility and is computed via sediment plasticity (plasticity index PI and/or liquid limit LL): low PI and high water content w (regarding liquid limit) are generally essential to increase liquefaction potential (Ghani and Kumari, 2020).

In the past decades, particle crushability has been thoroughly investigated in calcareous sands of different origins. Mechanical properties are heavily impacted by particle crushability (Wu et al. 2021; Coop 1990; Coop et al. 2004; Yu et al. 2019): high compressibility and increasing internal friction are some of the most published consequences. The literature consensus is that at the same relative density, remolded samples of carbonate sands tend to experience higher liquefaction resistance compared to silica sands. This is typically attributed to energy dissipation due to particle breakage and probable stress relaxation between loading cycles (Sandoval and Pando, 2012; Taylor and Green 2021; Hyodo et al., 2000; Brandes, 2011). Nevertheless, liquefaction due to large naturally deposited crushable particles imbedded in fine-particle matrices is poorly understood.

This study hypothesizes that the crushing of particles of biogenic origin is the microscale mechanism that promotes liquefaction at the macro-scale in natural sediments. Our goal is to (1) explore whether natural sediments with biogenic-origin particles can crush under external loading, and (2) evaluate the possibility that the crushability of these particles is the reason for enhanced liquefaction failure in naturally deposited carbonate layers in Mayotte submarine slopes. We first describe, characterize, and classify the recovered sediment cores. Then, we pursue the first goal using undisturbed samples under lab-controlled conditions in oedometer cells (K_0-conditions). Finally, we expand and corroborate our results with data for already liquefied samples reported in Sultan et al., (2023).

Geological Setting

The Comoros archipelago is located north of the Mozambique Channel (Indian Ocean), between Mozambique and Madagascar (Figure 1). The archipelago is composed of four volcanic islands (Grande Comore, Mohéli, Anjouan and Mayotte) aligned in an overall east–

west (E–W) trend (Daniel et al., 1972; Tzevahirtzian et al., 2021). The origin of volcanism in the area is not fully understood, although several hypotheses exist: (a) hot spot activity (Emerick and Duncan, 1982), (b) lithospheric fracture zones facilitating melt transport (Nougier et al., 1986), or (c) coupling of both processes, with the interaction of extensional tectonics and deeper astenospheric processes (e.g., Courgeon et al., 2018, Deville et al., 2018, Famin et al., 2020, Franke et al., 2015, Kusky et al., 2010, Michon, 2016, O'Connor et al., 2019, Wiles et al., 2020). More recently, Feuillet et al. (2021) suggested that the present-day morphology of the archipelago results from an E–W transtensional boundary that transfers the strain between the offshore eastern branch of the East-African rift and grabens off Madagascar.

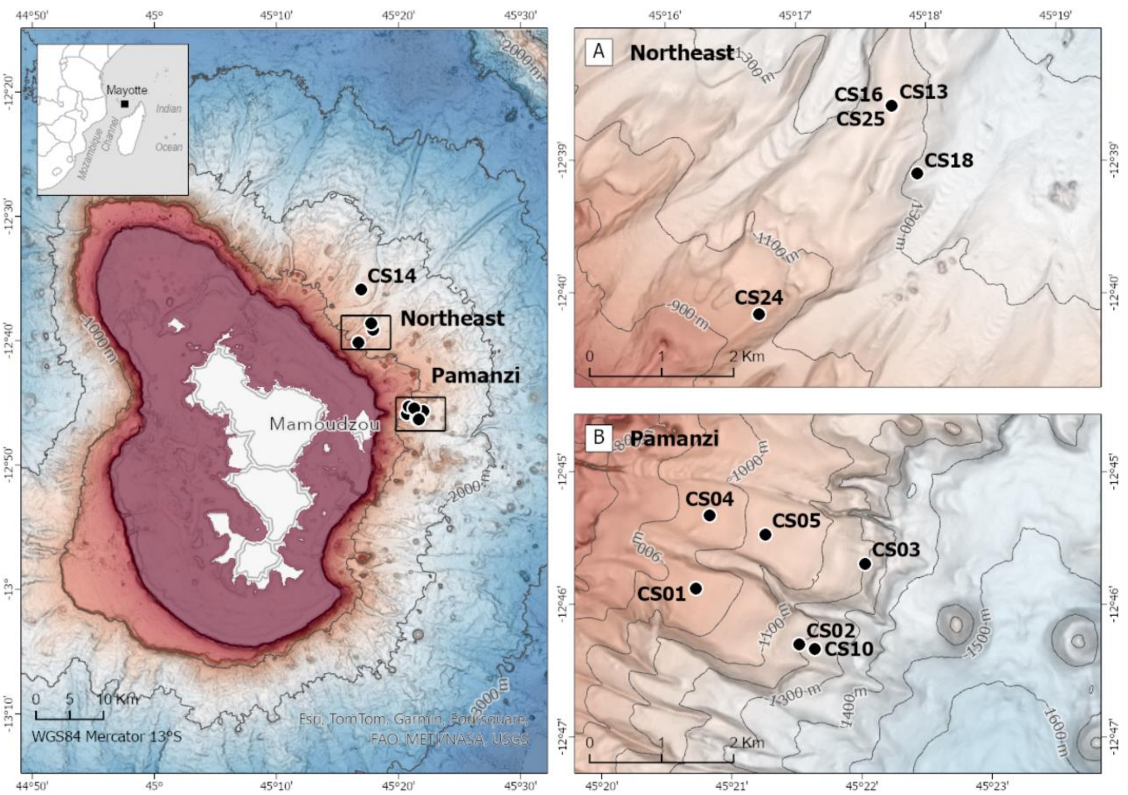

Figure 1: Bathymetry map and coring locations of Mayotte eastern slope: a) Northeast and b) Pamanzi areas (Rinnert et al. 2019). Data sources: SHOM 2016 bathymetry DTM (Homonim project) https://dx.doi.org/10.17183/MNT_MAY100m_HOMONIM_WGS84 and MAYOBS cruises

Recovered Cores, Sample Selection and Testing Methodologies

Recovered Cores and Testing Plan

The French Oceanographic Cruise MAYOBS19 recovered 25 Calypso piston cores for the characterization, classification, and study of sediment mechanical properties in two representative areas: Northeast and Pamanzi (Rinnert et al., 2021; Figure 1). Ranging from 2.25 up to more than 26 m long, each core was segmented onboard and stabilized at room temperature. Each segment was analyzed using a Multi-Sensor Core Logger (MSCL) to obtain magnetic susceptibility (MS), bulk density (γ-density), and P-wave velocity, achieving a spatial resolution of 1 cm. Figure 2 summarizes the values measured on the 12 cores used in this study, showing bulk density ranging from 1.55 to 1.85 g/cm^3, P-wave velocities from 1,455 to 1,800 m/s, and MS values between 1 and 1,300 SI (volume-based; Rinnert et al. 2021). Following the analysis methodology of Sultan et al. (2023), we classified the subsurface layers into carbonate- and volcanic-dominated sediments based on MS values, with values >100 indicating volcanic dominance. Of the 149 meters of cores recovered, we selected samples to represent different origins, densities, P-wave velocities, and magnetic susceptibilities. We named each sample as follows: CSXX-SYY-DDDD (where XX, YY and DDDD are the core number, section and depth in cmbsf respectively).

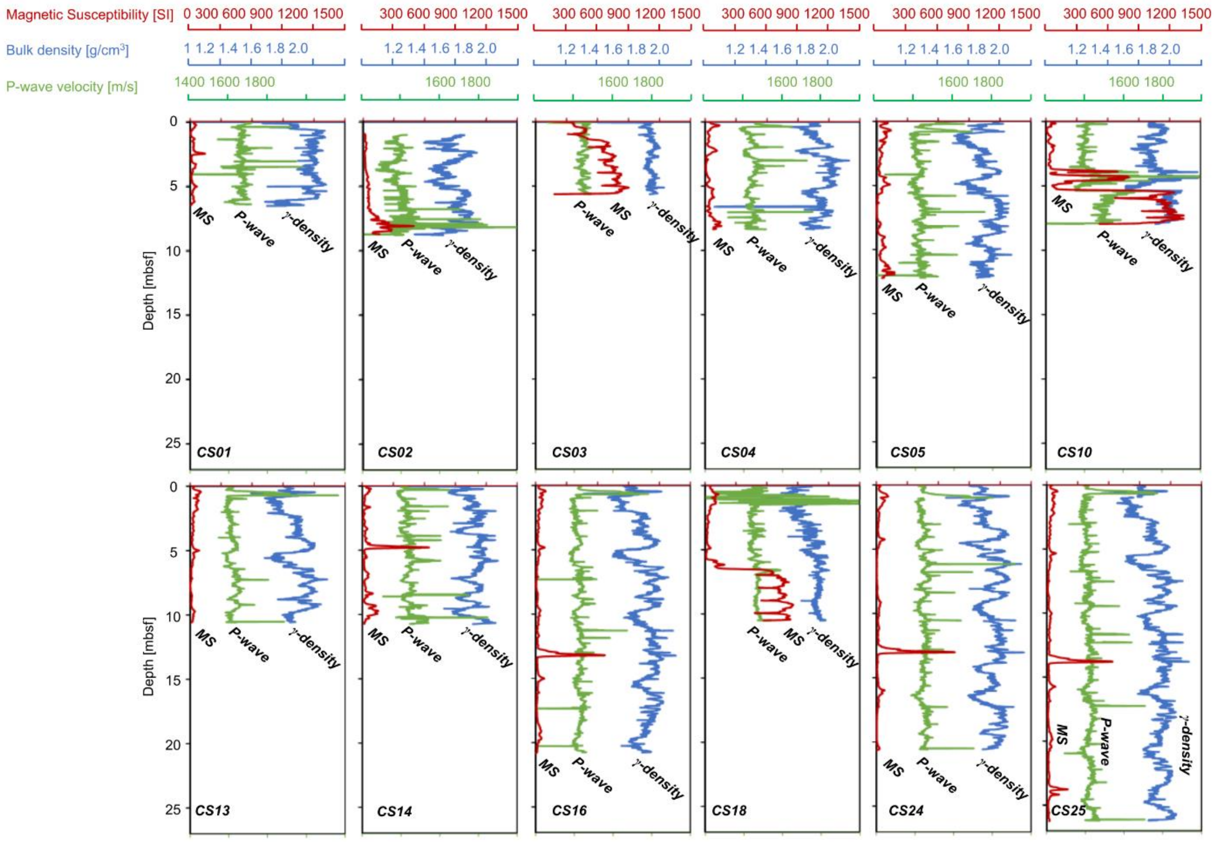

Figure 2: MSCL data from cores used in this study of magnetic susceptibility MS (red), bulk density γ-density (blue) and P-wave velocity (green). Colour-coded for the online version of this article.

A wide range of tests were performed to obtain several disturbed and undisturbed sediment properties, including (1) general characterization tests (specific gravity Gs, grain-size distribution, Scanning Electron Microscope SEM, Energy Dispersive X-ray Spectroscopy EDS, specific surface Ss, Atterberg limits); (2) engineering properties (K_0 compressibility, hydraulic conductivity k_{hyd}); (3) crushability under K_0 conditions. In addition, we determined crushability on samples subjected to liquefaction already published in Sultan et al. (2023). Although no liquefaction tests were performed in this study, we subsampled those already published in Sultan et al. (2023) and computed their post-test crushability. Subsequent sections review the test procedures, and Table 1 summarizes the tests performed, quantities, and typical results.

Table 1: Summary of lab tests conducted in this study

Category	Test	# samples	Typical results
Imaging	SEM (& selected EDS)	25	Biogenic (O, Ca, C) Magnetic inclusions (O, Si, Fe, Ti)
Index	Specific gravity *Gs*	38	Min = 2.69 ; Max = 2.91
	Specific surface *Ss*	38	Min = 4.7 m^2/gr ; Max = 43 m^2/gr
	Atterberg Limits *(LL, PL)*	33	LL = 49.5 to 90.9% PL = 34.35% to 73.7% Classification: SM or SC-MH (sandy silt)
	Grain size distribution	34	D_{50} = 22.8 to 129 µm D_{10} = 1.6 to 8.1 µm Cu = 14.5 to 52.5
	In-situ water content, *w*	38	w = 44.2 to 92.4%
Engineering	Compressibility	17	Cc = 0.07 to 0.37 Cv = 1.75 to 7.0 mm^2/s (*) $C\alpha^{mod}$ = 0.07 to 0.38 % (*)
	Hydraulic conductivity, k_{hyd}	17	$k_{ini} = 2 \cdot 10^{-5}$ to $9 \cdot 10^{-7}$ cm/s δ = 3.3 to 7.4
Specialized	Crushability at ko conditions	12	Crushability at σ' > 500 kPa
	Crushability post liquefaction	18	(**)

(*) computed at in-situ stress
(**) liquefaction tests were performed and published in Sultan et al. 2023. Results and testing conditions summarized in Supplementary Table SLT.

General Characterization

SEM and EDS

We photographed particle shapes and unique features with a Scanning Electron Microscope SEM Quanta 200 (Thermofisher, FEI). We used a sieve with an aperture of 63 µm to separate the larger grains. In the samples with high MS, we used a magnet to separate those with magnetic properties and then visually selected them for further imaging. Additionally, we applied the Energy-Dispersive Spectroscopy EDS capabilities of the Quanta 200 to qualitatively determine the most relevant chemical elements present in the carbonate and volcanic particles.

Specific Gravity Gs

Due to the variability of MS and bulk density measured in the cores, we obtained particle Gs from water-saturated samples according to ASTM D854-10 (ASTM, 2006).

Grain Size

We determined the distribution of soil particle size using laser granulometry (Malvern Mastersizer 3000). Each sample was tested three times to ensure reproducibility, repeatability and quality control. We used these three individual results to compute measurement errors. We adopted the Unified Soil Classification System USCS to prepare, test and classify these sediments.

Specific Surface Ss

The specific surface area S_S determines hydraulic conductivity, and controls advective-diffusive-reactive transport, electrical conductivity, and permittivity (Santamarina et al. 2002). We measured Ss of sediment samples using the colorimetry-based method with methylene blue (see details in Salva and Santamarina, 2021).

Atterberg Limits and Classification

We classified fine sediments according to USCS, as standardized in ASTM D2487-11 (ASTM, 2011a). We performed fall cone tests to determine the sediment Liquid Limit LL (BS1377-2, BS 1990) and the rolled-thread method to obtain the Plastic Limit PL (ASTM D4318, ASTM 2017).

Engineering Properties (undisturbed samples)

Sample Selection

We sub-selected six carbonate- and six volcanic-dominated samples to test their undisturbed engineering properties up to 1.7 MPa of vertical effective stress (K_0-conditions). The samples were selected to represent distinct values along the range of MS (17.6-832 SI), density (1.55-1.78 gr/cm^3), and P-wave velocity (1,489-1,534 m/s).

K_0 Compressibility

A standard oedometer cell was used to investigate the static consolidation of undisturbed samples according to ASTM D2435/D2435M-11 (ASTM, 2011b). We curve-fitted each loading stage to obtain primary consolidation Cv, and secondary consolidation Cα coefficients.

Hydraulic Conductivity

We obtained hydraulic conductivity on each loading step during K_0 compressibility in the standard oedometer cell via the falling-head method according to ASTM D5856 (ASTM 2015). To compare with worldwide databases, we curve-fitted it to a power law (Ren and Santamarina 2018): $k_{hyd} = k_{ini}\left(\frac{e}{e_o}\right)^{\delta}$, where k_{ini} is hydraulic conductivity at a reference void ratio ($e/e_0 = 1$), e_o is the initial void ratio and the δ-exponent is the sensitivity parameter.

Crushability

Quantification

To quantify crushability, we based our analysis on comparing grain-size distribution in undisturbed and post-test conditions. We considered three methods: (1) breakage index Bλ (Tong et al. 2022; Einav 2007), (2) the change in fines content, and (3) areas below the grain-size cumulative curve. We were not able to apply method (1) since it is based on the estimation of the ultimate grain-size distribution, which typically yields particle sizes larger than the natural measured distribution and results in negative breaking indices Bλ (see all results in Supplementary Figures SF). Conversely, method (2) may be biased toward large particle changes because changes in the range of small particles may not be as noticeable in the FC computation as with large particles. Thus, to simplify analysis and consider the small and large particles equally, we adopted method (3). We computed particle crushability from the ratio between areas:

$$\Delta Area\ [\%] = \frac{A_{post} - A_{und}}{A_{und}} \cdot 100\% \quad (1)$$

where A_{und} and A_{post} are the undisturbed and post-test area below the cumulative grain-size curves respectively.

Methodology and Sample Selection for Testing Under K_0-conditions

We first tested the crushability potential and load threshold of the natural Mayotte samples. From two distant cores, we selected one segment each at the same depth below the seafloor (i.e., same in-situ effective stress), similar values of MS, bulk density, and P-wave velocity to guarantee repeatability. Cores CS04 and CS13 at depths 4.95-5.22 mbsf met these criteria (see Figure 2 for MSCL data). Fines content of these samples were 40% ± 10% for both cores. We then sliced them into 5-cm segments and applied different, consecutive, and sequential effective stress in a standard oedometer cell (15, 25, 50, 100, 200, 500, 1,000, and 1,760 kPa).

Methodology and Sample Selection Subjected to Liquefaction

The Cyclic Resistance Ratio CRR is a measure of a soil's ability to resist liquefaction due to cyclic loading. We selected 18 already liquefied samples for crushability quantification at different cyclic resistance ratios (liquefaction test results, in-situ density, confinement stress, CRR computation and other details can be found in Sultan et al. 2023 and are summarized in Supplementary Liquefaction Table SLT) to represent a comprehensive range of fines content and CRR. To simplify our analysis, we combined the cyclic resistance ratio and cycle number to liquefaction N into a unique parameter C as proposed and reported in Sultan et al. (2023). For Mayotte slope sediments, $C = CRR/N^{-0.13}$. With this normalization, C becomes a function of lithology, incorporating sediment density and magnetic susceptibility.

Results and Analyses

Table 1 summarizes typical results, while Supplementary Results Table SRT, Supplementary Figures SF and Supplementary Material SM compile the results and group the raw data from every test respectively. The following sections review each individual test results and analyses.

Sediment Characterization and Classification

SEM and EDS.

Photographs of carbonate-dominated sediments show a prevalence of biogenic origin particles (foraminifera, mollusk shells and echinoids) of large size (> 63 μm) within a fine matrix (Figure 3). They display a porous structure with internal, potentially accessible porosity. In all samples, these weak shells show a degree of breakage (last row in Figure 3). Conversely, volcanic-dominant samples are characterized by biogenic-based matrices with inclusions of magnetic particles of regular shape (euhedral, tetrahedral, or octahedral) and rounded edges. EDS results (Supplementary Material EDS) denote that carbonate-dominated sediments are rich in Oxygen (range: 50-59%), Calcium (29-48%) and Carbon (0-11%) while in magnetic particles, their chemical composition is Oxygen (31-55%), Silica (0-22%), Iron (4-39%), and Titanium (1-16%).

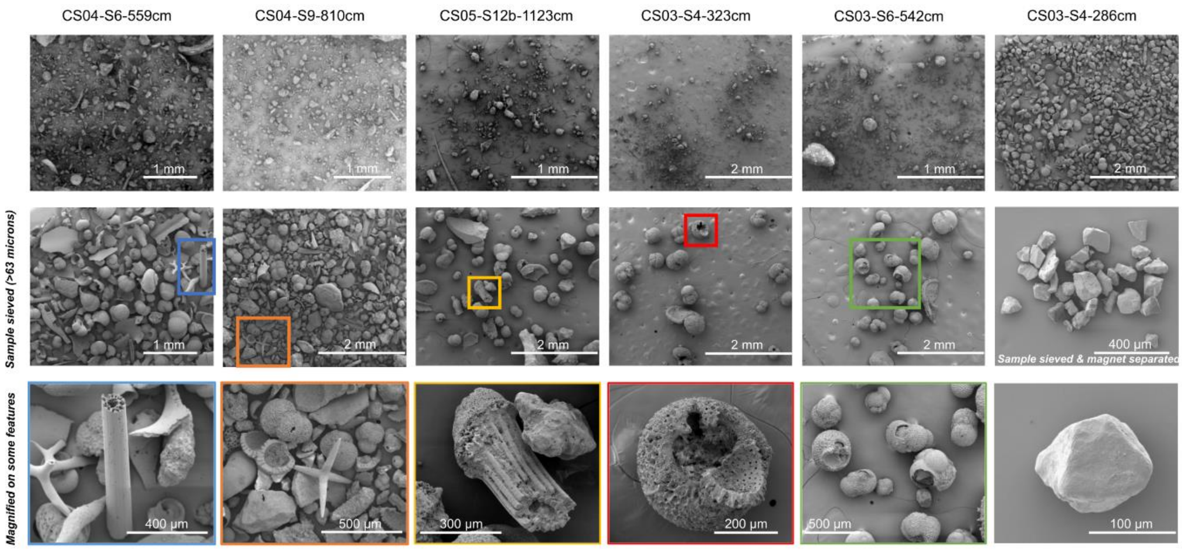

Figure 3: SEM images of selected samples. First five columns are carbonate-dominant while the sixth is volcanic-dominant. First row is the image of the sediment as initially sampled, the second row after sieving (> 63 μm) and the third row depicts unique features.

Specific Gravity

Figure 4 shows the measured specific gravity Gs of the carbonate- and volcanic-dominated sediments compiled in this study. Gs spans from 2.69 up to 2.91 and illustrates the impact of particle mineralogy. Carbonate-dominated samples typically comprise Calcite (Gs = 2.71) up to Aragonite (Gs = 2.83). Conversely, we observe a tendency towards higher Gs for volcanic-dominant sediments likely due to an increase in heavier minerals such as Fe.

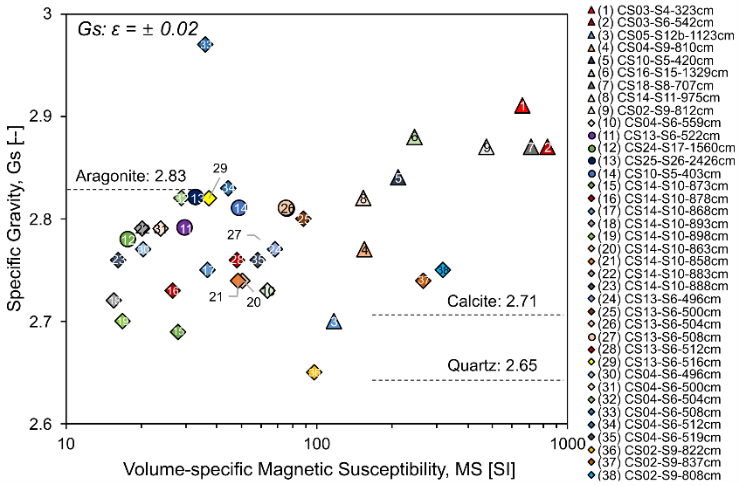

Figure 4: Specific gravity Gs vs. magnetic susceptibility MS results for all tests in this study. An increase of magnetic particles shifts Gs upwards, even beyond Aragonite typical values. Triangle symbols denote volcanic-dominated samples, while circles and diamonds are carbonate-dominated sediments. Specific gravity and magnetic susceptibility error are smaller than the symbol size, thus not shown in the graph. Colours in the online version and numbers are consistent with those in the other figures in this article.

Grain-size Distribution

Particle size distribution shows a bi-modal pattern for both carbonate- and volcanic-dominated sediments (Figure 5). Both sediments have a similar range of particle sizes (however, the latter has more fines) and the highest peak is in the range of 80-200 μm while the second highest is in the order of 2-10 μm. D_{50} spans from 22.8 to 129 μm, D_{10} from 1.6 to 8 μm while the coefficient of uniformity Cu extends from 14.5 to 52.5. By comparing the photographs of the sieved samples shown in Figure 3, we conclude that the highest peak of the bi-modal distribution corresponds to biogenic particles surrounded by a silty matrix.

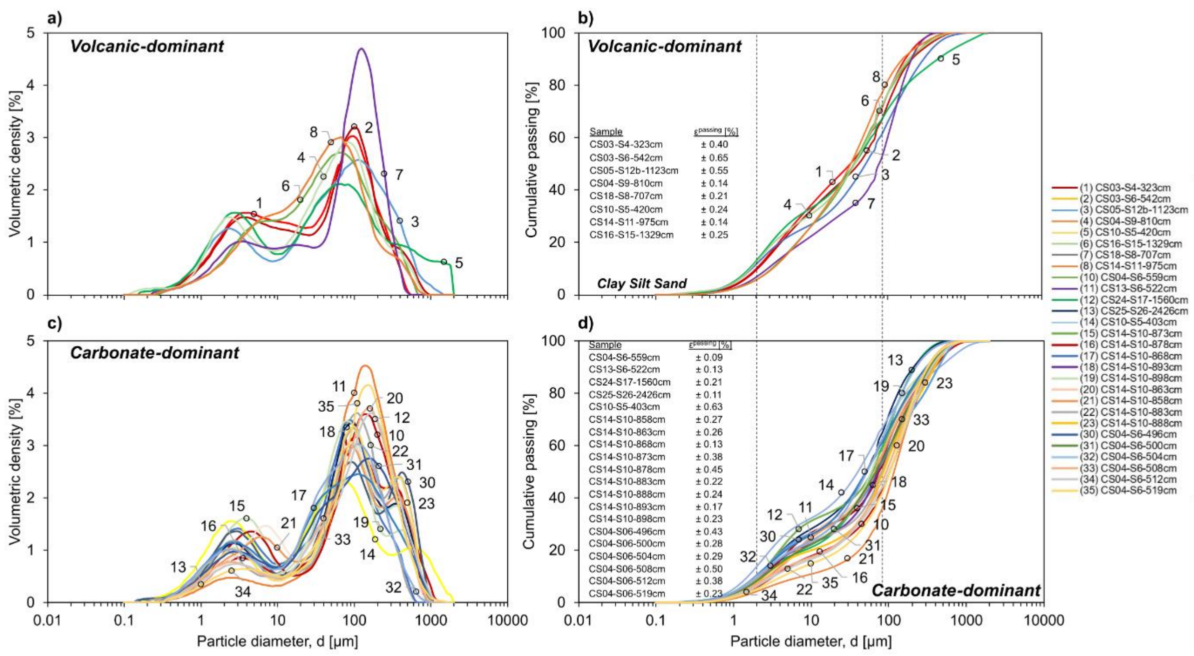

Figure 5: Grain-size distribution of carbonate- and volcanic-dominated sediments: a) and b) represent the volumetric density and cumulative passing for volcanic-dominant samples; while c) and d) are for carbonate-dominant samples. Each line depicts the average of three independent measurements for each sample, while the table insert summarizes the error in each test. Colours in the online version and numbers are consistent with those in the other figures in this article.

Measurement errors computed as explained in the Testing Methodology section are compiled in Figure 5. Typically, errors range from ±0.09% up to ±0.65%. Measurement errors in carbonate- and volcanic-dominant samples are in similar ranges, thus they are not origin-related.

Atterberg Limits Classification and Specific Surface

The sediments exhibited low and medium plasticity (PI ranges from 3.6% up to 30%) and were below the A-line (LL > 49.5%; Figure 6-a). Note that most volcanic-dominated sediments tend to have higher plasticity due to high fine content FC. Samples are classified as SC-MH/OH or SM-MH/OH (sandy silt). Specific surface results are compiled in Figure 6-b and they range from 4.7 up to 43 m^2/gr. Most sediments cluster around kaolinite-like soils but plot off-trend from LL and Ss data, likely due to saturated internal grain porosity (i.e., higher water intake). Additionally, methylene blue absorption by the silty matrix shifts Ss values toward those of kaolinite-like materials.

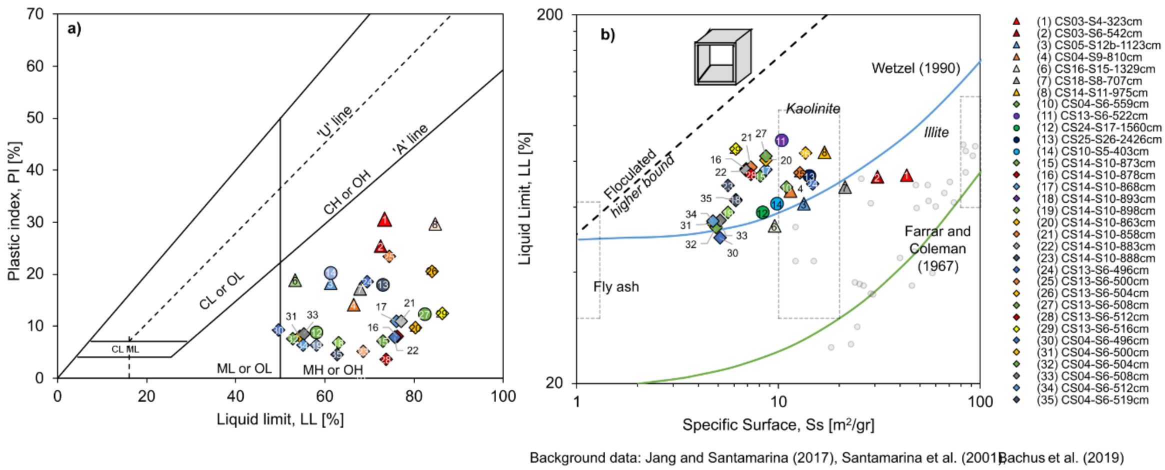

Figure 6: Mayotte's samples water interaction: a) Atterberg limits (Casagrande chart) and b) specific surface. Most of samples show a LL > 49.5% but below the A-line. Note that volcanic samples tend to have higher PI compared than the average for carbonate-dominant samples. Specific surface results cluster near kaolinite-like sediments in the worldwide database. Note that most datapoints show a high LL and high Ss respect to literature trends, likely showing that internal porosity water intake shifts the natural LL for these sediments. Triangle symbols denote volcanic-dominated samples, while circles and diamonds are carbonate-dominated sediments. Colours in the online version and numbers are consistent with those in the other figures in this article.

Engineering Properties

K_0 Compressibility

The results of the 12 samples tested in this study are compiled in Figure 7. We computed the compressibility index Cc, primary and secondary consolidation coefficients Cv and Cα at in-situ stress (in this study ≤ 100 kPa). Among all tested samples, Cc ranged between 0.07-0.15; Cv from 3.25 mm^2/s to 7.0 mm^2/s and Cα from 0.1% to 0.16%. Since the swelling index Cs depends on the maximum applied load, we do not report this value. Individual results for each sample can be found in the Supplementary Figures SF. Primary and secondary consolidation coefficients, and compressibility indices plot off the generally accepted trends and databases for fines and clays (Figure 7-b, -c, and -d). Since most of them are based on water content measurements (void ratio e, LL, in-situ water content w), we speculate that the internal particle porosity hosts water which increases w and LL with respect to typical solid quarzitic soils. Supplementary Results Table SRT compiles the results for all tests.

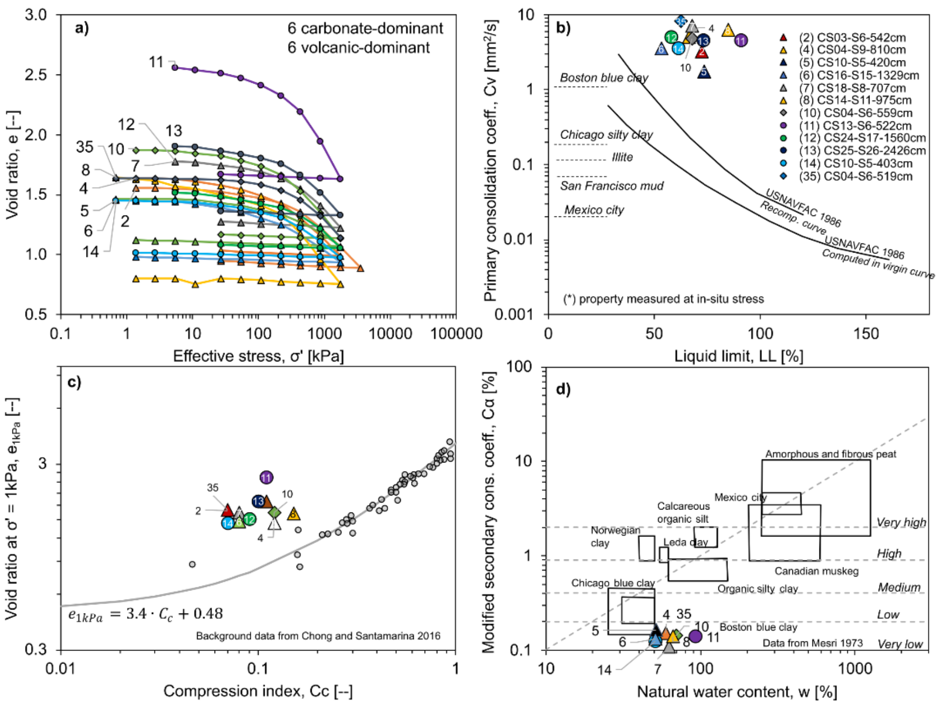

Figure 7: Consolidation and compressibility results: a) compressibility curves; b) primary consolidation and liquid limit trend superimposed to typical trends (NAVFAC 1986); c) compressibility index Cc and void ratio at 1 kPa e_{1kPa}; d) modified secondary consolidation coefficient $C\alpha^{mod} = C\alpha[\%]/(1+e_0)$. Cc, Cv and Cα were computed at in-situ stress. Triangle symbols denote volcanic-dominated samples, while circles and diamonds are carbonate-dominated sediments Colours in the online version and numbers are consistent with those in the other figures in this article.

Hydraulic Conductivity

Figure 8 shows the hydraulic conductivity of the 12 undisturbed samples measured in this study. Measurements plot similar to clay/silt-like soils when superimposed on the published databases (Figure 8-a). We report the initial hydraulic conductivity k_{ini} and δ-exponent (Figure 8-b and -c) to summarize the hydraulic behavior on loading. In all cases, k_{ini} and δ cluster on clayey-like soils. Supplementary Figure SF compiles all tests conducted.

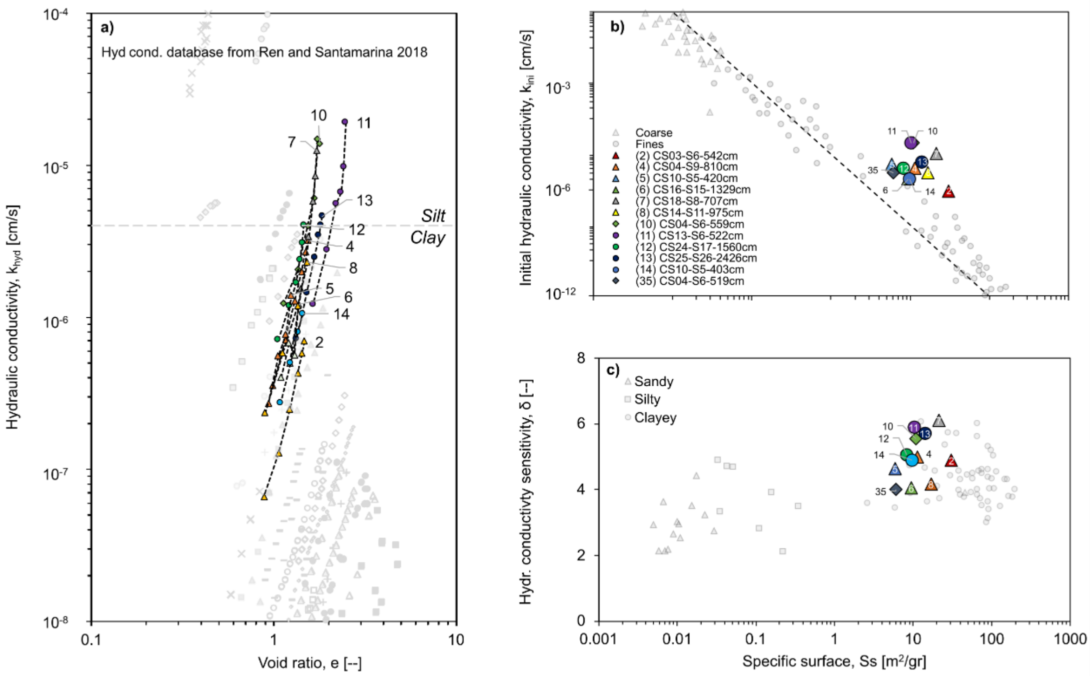

Figure 8: Hydraulic conductivity (undisturbed samples) superimposed to published soils databases (Ren and Santamarina 2018): a) raw data; b) initial hydraulic conductivity k_{ini} and c) sensitivity exponent δ against specific surface Ss. Colours in the online version and numbers are consistent with those in the other figures in this article.

Liquefaction susceptibility

We evaluated the potential for liquefaction of the tested samples according to 13 different indirect criteria (Table 2) and arranged them from the most to least restrictive (i.e., those with a relatively lax criteria on liquefaction susceptibility). There is no consensus that any sample is susceptible to liquefaction among all criteria; however, the least restrictive (i.e., criteria [7] to [13] in Table 2) highlight those samples as susceptible to liquefaction since they present low fines and high-water content with respect to the liquid limit.

Table 2: Liquefaction susceptibility

Sample	w [%]	LL [%]	PL [%]	PI [%]	< 5 µm [%]	< 2 µm [%]	[1]	[2]	[3]	[4]	[5]	[6]	[7]	[8]	[9]	[10]	[11]	[12]	[13]
CS03-S4-323cm	58.9	73.4	41.7	30.6	24.4	9.5	NS	NS	NS	NS	NS	NS	NS	NS	NS	NS	NS	NS	NS
CS03-S6-542cm	61.4	72.5	47.2	25.4	23.2	9.0	NS	NS	NS	NS	NS	NS	NS	NS	NS	NS	NS	NS	NS
CS05-S12b-1123cm	57.1	61.2	42.9	18.3	22.1	11.2	NS	NS	NS	NS	NS	NS	PS	NS	NS	NS	NS	NS	NS
CS04-S6-559cm	69.5	67.9	NP	N/A	14.0	5.8	S	NS	NS	NS	NS	NS	NS	S	NS	NS	NS	NS	NS
CS04-S9-810cm	59.4	66.4	52.3	14.1	16.3	5.5	NS	NS	NS	NS	NS	NS	PS	NS	NS	NS	NS	MS	S
CS13-S6-522cm	92.4	90.9	NP	N/A	8.8	4.3	S	NS	NS	NS	NS	NS	NS	S	NS	NS	NS	NS	NS
CS18-S8-707cm	62.1	67.9	50.7	17.2	16.2	6.5	NS	NS	NS	NS	NS	NS	PS	NS	NS	NS	NS	MS	NS
CS24-S17-1560cm	55.5	58.1	49.3	8.8	17.8	10.0	NS	NS	NS	NS	NS	NS	S	NS	NS	NS	NS	S	S
CS25-S26-2426cm	68.0	73.0	55.0	18.0	22.7	9.5	NS	NS	NS	NS	NS	NS	PS	NS	NS	NS	NS	NS	NS
CS10-S5-403cm	50.7	61.3	41.0	20.3	27.5	13.7	NS	NS	NS	NS	NS	NS	NS	NS	NS	NS	NS	NS	NS
CS10-S5-420cm	51.7	N/A	N/A	N/A	27.0	12.5	ND	ND	ND	ND	ND	ND	ND	ND	NS	NS	NS	ND	NS
CS16-S15-1329cm	50.8	53.3	34.4	18.9	24.7	11.9	NS	NS	NS	NS	NS	NS	PS	NS	NS	NS	NS	NS	NS
CS14-S11-975cm	66.1	84.7	55.0	29.6	15.9	5.5	NS	NS	NS	NS	NS	NS	NS	NS	NS	NS	NS	NS	NS
CS14-S10-873cm	71.4	72.9	65.2	7.1	24.3	9.3	NS	NS	NS	NS	NS	NS	S	NS	NS	NS	NS	S	S
CS14-S10-878cm	71.0	76.1	68.1	8.0	19.8	7.4	NS	NS	NS	NS	NS	NS	S	NS	NS	NS	NS	S	S
CS14-S10-868cm	73.2	75.9	64.8	11.0	21.9	9.4	NS	NS	NS	NS	NS	NS	S	NS	NS	NS	NS	S	S
CS14-S10-893cm	59.8	63.0	56.2	6.8	18.8	8.6	NS	NS	NS	NS	NS	NS	S	NS	NS	NS	S	S	S
CS14-S10-898cm	55.9	58.1	51.7	6.4	19.1	9.6	NS	NS	NS	NS	NS	NS	S	NS	NS	NS	S	S	S
CS14-S10-863cm	75.2	80.3	70.7	9.7	16.3	6.1	NS	NS	NS	NS	NS	NS	S	NS	NS	NS	NS	S	S
CS14-S10-858cm	70.6	77.0	65.9	11.0	16.9	6.7	NS	NS	NS	NS	NS	NS	S	NS	NS	NS	NS	S	S
CS14-S10-883cm	69.9	75.6	67.7	7.9	19.4	8.8	NS	NS	NS	NS	NS	NS	S	NS	NS	NS	NS	S	S
CS14-S10-888cm	64.8	68.6	63.4	5.2	16.7	7.6	NS	NS	NS	NS	NS	NS	S	NS	NS	NS	S	S	S
CS13-S6-496cm	56.5	69.5	50.9	18.6	20.9	10.1	NS	NS	NS	NS	NS	NS	PS	NS	NS	NS	NS	NS	NS
CS13-S6-500cm	58.1	74.4	51.0	23.4	17.4	8.1	NS	NS	NS	NS	NS	NS	NS	NS	NS	NS	NS	NS	NS
CS13-S6-504cm	67.6	84.0	63.4	20.6	19.2	9.8	NS	NS	NS	NS	NS	NS	NS	NS	NS	NS	NS	NS	NS

CS13-S6-508cm	70.7	82.3	70.0	12.3	14.1	7.0	NS	NS	NS	NS	NS	NS	PS	NS	NS	NS	NS	MS	S
CS13-S6-512cm	69.7	73.6	70.0	3.6	13.1	6.2	S	NS	NS	NS	NS	NS	S	S	S	S	S	S	S
CS04-S6-496cm	44.2	49.5	40.2	9.3	20.9	10.1	NS	NS	NS	NS	NS	NS	S	NS	NS	NS	NS	S	S
CS04-S6-500cm	50.2	54.3	46.2	8.1	17.4	8.1	NS	NS	NS	NS	NS	NS	S	NS	NS	NS	NS	S	S
CS04-S6-504cm	48.0	52.8	45.1	7.6	19.2	9.8	NS	NS	NS	NS	NS	NS	S	NS	NS	NS	NS	S	S
CS04-S6-508cm	49.9	55.2	46.6	8.5	14.1	7.0	S	NS	NS	NS	NS	NS	S	S	NS	NS	NS	S	S
CS04-S6-512cm	52.7	55.0	48.6	6.4	13.1	6.2	S	NS	NS	NS	NS	NS	S	S	NS	NS	S	S	S
CS04-S6-519cm	59.3	62.6	58.0	4.6	11.2	5.0	S	NS	NS	NS	NS	NS	S	S	NS	NS	S	S	S

S: Susceptible; NS: Non-susceptible; PS: potentially susceptible; MS: moderately susceptible; ND: no sufficient data to compute; w: water content; LL: liquid limit; PL: plastic limit; PI: plasticity index

References and liquefaction susceptibility criteria: [1] Seed and Idriss (1982): 5µm < 15% & LL < 35 & w/LL > 0.9; [2] Youd (1998): PI < 7% & LL < 35% & Plot below A-line; [3] Andrews and Martin (2000): 2 µm < 10% & LL < 32%; [4] Polito (2001): LL < 25% & PI < 7%; [5] Seed et al. (2001): LL < 30% & PI < 10%; [6] Seed et al. (2003): LL < 37%. & PI < 12% & w/LL > 0.8; [7] Bray et al. (2004) PI < 12% & w/LL > 0.85; [8] "Chinese criteria" – Wang (1979): 5µm < 15% & w/LL > 0.9; [9] Prakash and Sandoval (1992): 2 < PI < 4%; [10] Ishihara and Koseki (1989): PI < 4%; [11] Boulanger and Idriss (2006): PI < 7%; [12] Bray and Sancio (2006): PI < 12%; [13] Gratchev et al. (2006): PI < 15%

Particle Crushability

We quantify particle crushability as a consequence of static or cyclic loading via grain-size distribution pre- and post-test. Figure 9 shows two typical examples of carbonate- and volcanic-dominant sediments (in color for the average of three measurements and in grey the raw data). In both cases, grain-size distribution is impacted by the applied effective stress, showing differences between undisturbed and post-test grain sizes for particles larger than 10 µm (Figure 9a and 9c). By comparing undisturbed and post-test results in carbonate-dominant samples, the large particle peak shifts to the left (black arrow in Figure 9a) and the distribution becomes wider. In volcanic-dominant samples, the large particle peak does not shift towards smaller particle sizes; however, it does widen. We associate this effect with a higher variability in particle diameter >500 µm, which is likely due to their natural heterogeneity (see grey lines in Figure 9c; for more examples see Supplementary Material SM). The curve shift mentioned above is also shown in the cumulative curves in Figure 9b and 9d for carbonate- and volcanic-dominant samples.

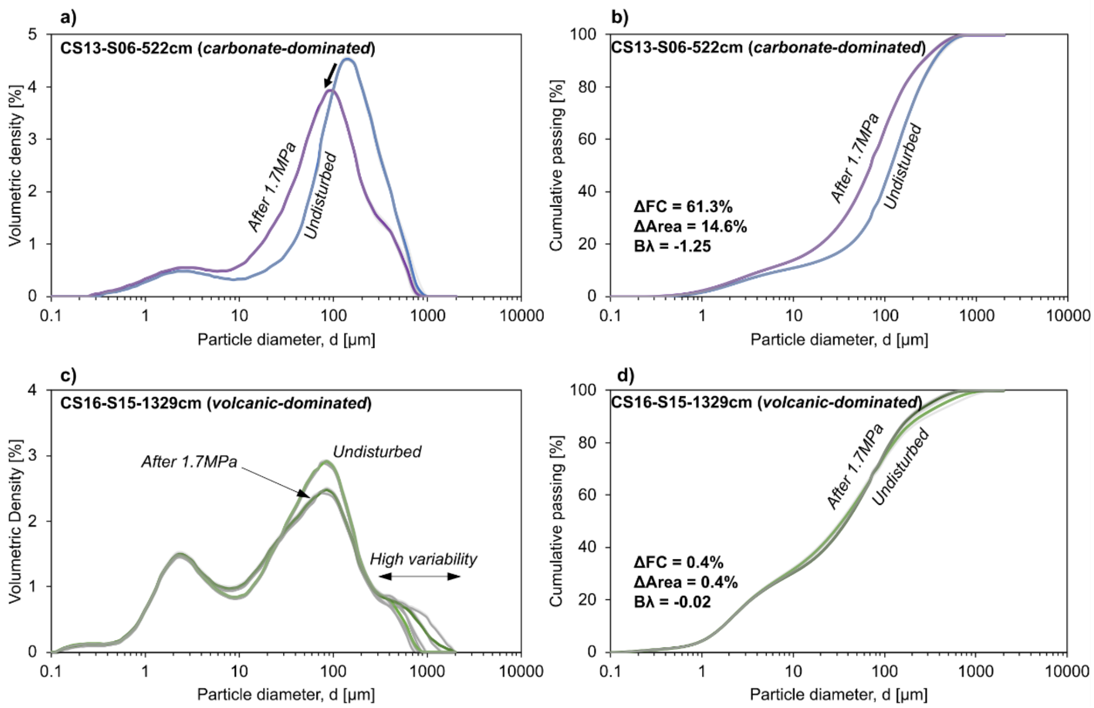

Figure 9: Grain-sizes of two typical examples pre and post application of 1.7 MPa of vertical effective stress: a) and b) volumetric density and cumulative passing curves for a carbonate-

dominant sample; c) and d) volumetric density and cumulative passing curves for a volcanic-dominant sample. Passing refers to the cumulative passing results from the grain-size distribution curves. Insert information are the computed crushability with the three methods. Grey lines represent raw measured data while colored lines (in the online version) are the average in distribution or cumulative at each individual particle diameter.

The consequence of the curve shifting of large particles towards smaller particles suggests that only they crush under the applied load. By comparing the SEM images in Figure 3, it is clear that biogenic-origin particles are the most impacted by crushing. This is also supported by comparing fines content (FC) with crushability (ΔArea) (Figure 10): an increase in the amount of large biogenic particles (i.e., a decrease in FC) increases crushability. Finally, our results highlight that even at a high amount of FC, crushability plays an important role in sediment behavior.

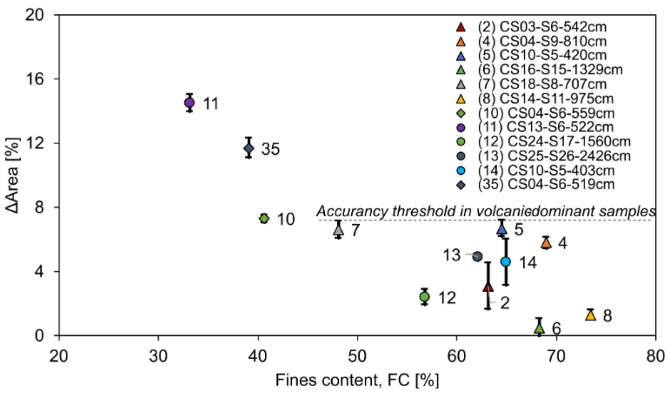

Figure 10: Impact of fines content in particle crushability. Error bars denote the variability on the measurement in GSD. Error in fines content FC is less than the width of the marker therefore not shown. Triangle symbols denote volcanic-dominated samples, while circles and diamonds are carbonate-dominated sediments. Colours in the online version and numbers are consistent with those in the other figures in this article.

Regarding measurement errors, it is important to note that even though the overall individual measurement error is low (Figure 5), when ΔArea is computed for different combinations of grain-size cumulative curves, this value can substantially increase. Thus, to avoid the impact of local heterogeneities (and potential negative values), we adopt the largest computed error of 7% for volcanic-dominant samples as the acceptance threshold. This variability was not found in carbonate-dominant samples; therefore, we adopt the errors as computed in these sediments. Note that all volcanic-dominant samples fall below the acceptance threshold in Figures 10, 11, and 13.

Even though our results suggest that the consequence of a load application is the crushing of biogenic particles, we considered other potential sources of crushability: sampling disturbance, fast unloading (in the case of gas presence), and subsampling. We mitigated these by working on the sediments at the center of the coring tube, purposely slowly removing the load from the sample (even though there was no gas present in the samples), and carefully subsampling the center of each sample by gently removing sediments layer by layer. Additionally, we considered cementation as a potential factor impacting Mayotte's sediment behavior; however, it was not observed in any of the SEM images (undisturbed, disturbed, or sieved; Figure 3).

Impact of Crushability on Engineering Properties

The 12 undisturbed sediments in this study classify as sandy silts with some behavioral features of clays (Figures 6 to 8). Figure 11 compiles the results of load-dependent engineering properties: permeability sensitivity δ, compression index Cc, primary consolidation Cv, and secondary consolidation Cα. We observe a clear trend along particle crushability for carbonate-dominant sediments only, suggesting that crushability plays an important role in naturally-deposited carbonates and the use of physical properties for engineering design should take into consideration the final applied load for the purpose of this study. Finally, we estimated the cyclic resistance ratio CRR as suggested by Sultan et al. (2023) for N = 15 for the 12 samples (Figure 12). As observed in static engineering properties, CRR aligns well with particle crushability for carbonate-dominated sediments (R^2 = 0.87), thus suggesting that particle crushability might promote liquefaction.

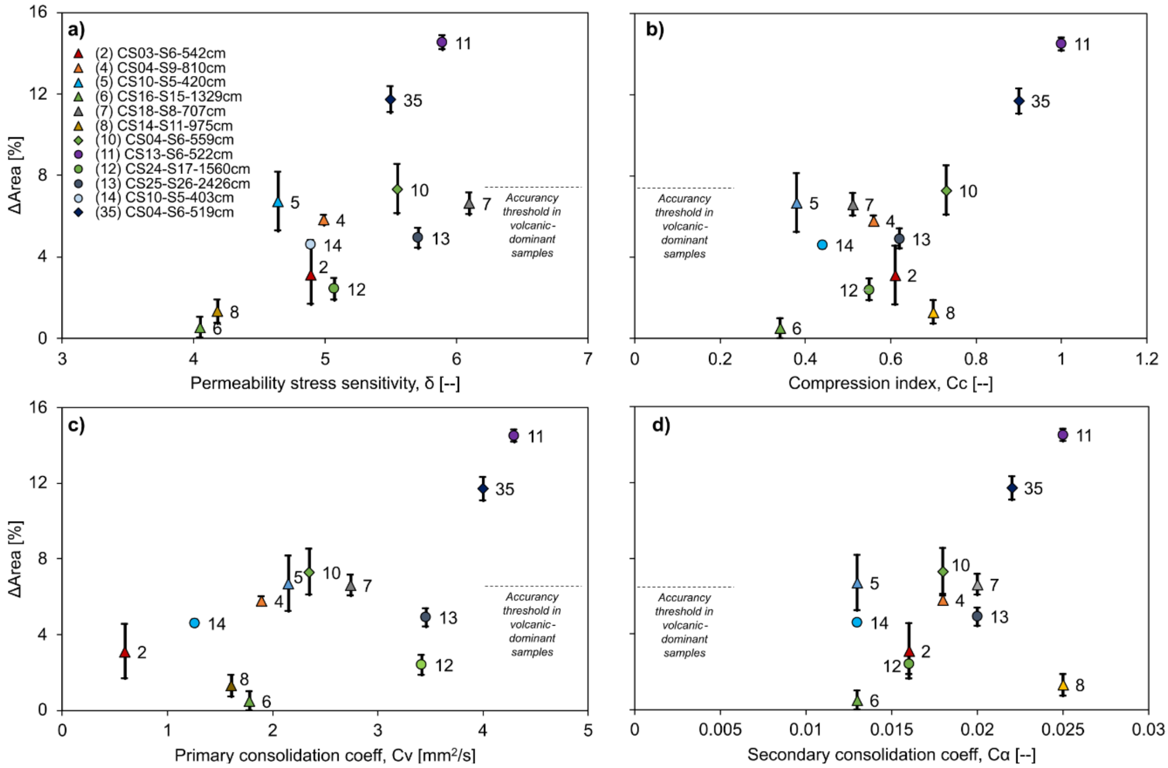

Figure 11: Impact of particle crushability on engineering properties of natural carbonate sediments at in situ effective stress: a) hydraulic conductivity sensitivity δ; b) compression index Cc; c) primary consolidation coefficient Cv and d) secondary consolidation coefficient Cα. Triangle symbols denote volcanic-dominated samples, while circles and diamonds are carbonate-dominated sediments. Colours in the online version and numbers are consistent with those in the other figures in this article.

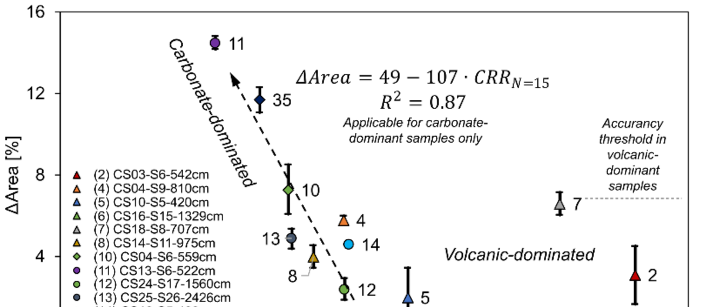

Figure 12: Estimated cyclic resistance ratio CRR for 15 cycles (N = 15) and particle crushability of Mayotte's slope samples. Triangle symbols denote volcanic-dominated samples, while circles and diamonds are carbonate-dominated sediments. Colours in the online version and numbers are consistent with those in the other figures in this article.

Stress-dependent Crushability Under K_0 conditions

We investigated the load threshold of particle crushability for carbonate-dominant sediment samples by applying progressively increasing effective stress loads to lithologically similar undisturbed samples. The results in Figure 13 show a clear threshold at ~500 kPa, tripling the crushability ΔArea beyond this value. This breakage threshold considers the low FC values of these samples (FC = 40% ± 10%), the low strength of the carbonate material, and the high porosity and shape variability of biogenic particles. In addition, this crushability depends on the stress path, where, for instance, triaxial tests produce more grain breakage than one-dimensional compression tests (Daouadji et al., 2001).

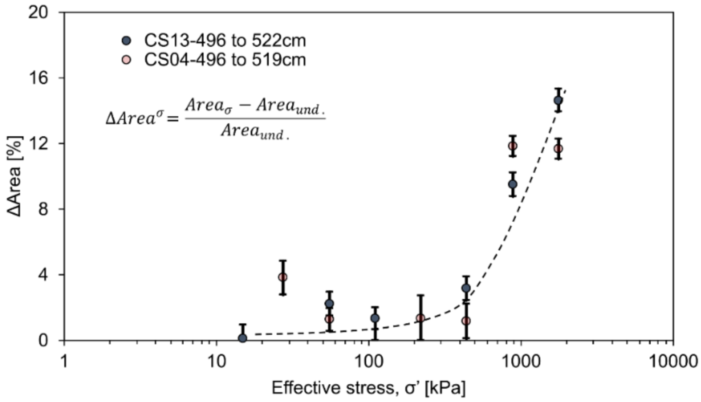

Figure 13: Stress-dependent particle crushability in naturally deposited carbonate-dominant sediments.

Crushability – Post liquefaction

Following the analysis described above, we applied the most meaningful parameters to corroborate crushability as the source of liquefaction: fines content, particle crushability, origin, and cyclic resistance ratio (Figure 14). We subsampled already liquefied samples published in Sultan et al. (2023), and obtained the grain-size distribution (in undisturbed conditions and post-test) to compute their post-test crushability. We observed a similar trend with respect to the undisturbed static results (Figure 14a, 14b,14c): an increase in crushability as fines content decreases for carbonate particles even up to 60% of fines content. Volcanic-dominant particles do not seem to be as impacted, likely due to their high fines content, particle size variability, and inclusion of solid magnetic particles. Our results suggest that the local crushability of particles represents the micro-scale behavior that evolves into liquefaction at the macro-scale.

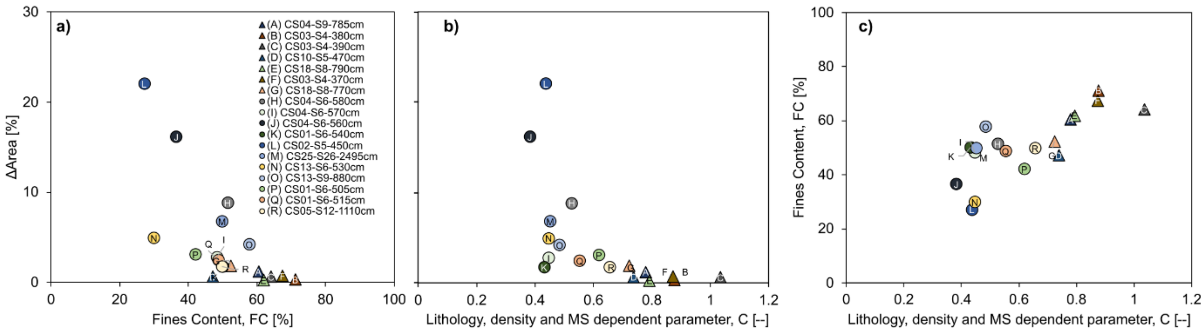

Figure 14: Compilation of crushability results post-liquefaction tested in Sultan et al. (2023) regarding fines content FC, cyclic response factor $C = CRR/N^{-0.13}$ and particle crushability ΔArea and their interaction: a) fines content vs. crushability; b) cyclic response factor vs crushability; c) fines content vs cyclic response factor. Error bars are not shown due to visualization superposition; however, note that the maximum error is ±1.2% in ΔArea. Triangle symbols denote volcanic-dominated samples, while circles and diamonds are carbonate-dominated sediments.

Discussion and Implications

Classification of Naturally Deposited Biogenic Particles

Classical geotechnical soil classification methods such as USCS relies on particle size, liquid limit and plastic limit. However, the inherent inner open structure of biogenic particles allows for a higher water intake and therefore bias the estimation of water-based measurements. Our results show that most of the tested sediments classify as sandy silts; however, their engineering properties are plotting off-trend from worldwide databases and generally accepted correlations, sometimes even behaving as clay-like soils. Clearly, standard classification methods are very limited for sediments of biogenic-origin and classical correlations should be discouraged.

Biogenic Particles as Failure Mechanism under Static Loading

Grain crushability can occur under static loading. Data in Figure 13 show that there is a threshold stress that could accelerate this crushability and potentially degrade the mechanical properties of the sediment. The breakage threshold stress found in this study is lower than individual particle breakage stress levels reported in the literature for particles of similar origin (1.6 MPa; Beemer et al., 2019; Mohtashami et al., 2023). This suggests a mechanism of force concentration or localization in naturally-deposited open-structure sediments, likely due to local accumulations of coarse particles.

The threshold stress found in this study depends on the loading path (Daouadji et al., 2001) but also on the strength of carbonate material, initial porosity, and the shape variability of biogenic particles. It is plausible that crushability beyond this threshold stress weakens the sediment and creates layers susceptible to generate strain localization and failure under static loading. This could, for instance, be the cause of some of the numerous slope instabilities shaping the Mayotte continental slope (Sultan et al., 2023).

Biogenic Particles as Failure Mechanism for Liquefaction

Literature shows that the presence of sandy soils (or coarse particles with very low fines content) is necessary for the liquefaction process to occur. Additionally, typical methodologies for evaluating liquefaction susceptibility cannot unequivocally conclude on the liquefaction potential of Mayotte's sediments (Table 2). However, combining our results with those already published for Mayotte’s slopes shows that (1) Mayotte's samples can liquefy even with high fines content; (2) lithology and the content of biogenic-origin sediment particles promote the liquefaction of Mayotte’s offshore sediments; and (3) particle crushability promotes liquefaction. Thus, liquefaction susceptibility methods developed for quarzitic soils cannot be applied to natural biogenic sediments.

Several studies on the crushability of remolded calcareous sandy soils have concluded that as particles break, the overall resistance to liquefaction increases (for the same relative density; Sandoval and Pando, 2012; Brandes 2011). Contrary to these findings, our results show the opposite trend. A potential explanation is that weak biogenic particles "floating" in a matrix of fines (or a local accumulation of biogenic particles) collapse or break upon the application of a monotonic or cyclic load which suddenly modifies the void ratio and generates a local spike in pore pressure that the fine matrix cannot dissipate, thereby promoting liquefaction. Nevertheless, this explanation should be carefully tested and evaluated, and complemented through imaging (μCT) and/or simulated via DEM (Discrete Element Modeling). See also the discussion below and the shape of the grains.

Implications for Wind Farms

The behavior of calcareous sands and carbonated sediments, which are abundant in tropical seas, can affect the design and long-term stability of offshore engineering structures (Shahnazari et al., 2016). For instance, driven piles in calcareous sands are known to have lower capacity than in siliceous sands (Murff, 1987; Nauroy and LeTirant 1985), leading to the use of expensive drilled and grouted piles with higher capacities. The long-term performance of a wind turbine foundation in such environments under the repeated cyclic and dynamic loads generated by wind, waves, rotor, and blade rotations is a major engineering problem in the field (Wang et al., 2021). The limited number of investigations carried out on the liquefaction potential of calcareous sand often conclude that this type of sediment has a much lower liquefaction potential than siliceous sands (Hyodd et al., 1998; LaVielle, 2008; Sandoval and Pando, 2012; Shahnazari et al., 2016). The question that arises is whether it is possible to generalize this observation concerning liquefaction potential. It is evident from our results that such a conclusion is not accurate, as our data demonstrate that the crushability of the tested carbonate-dominated sediments promotes liquefaction. This result seems coherent with the explanation that the interstitial pore-pressure leading to liquefaction is a function of the sand's tendency to compress when a load is applied (Seed and Lee, 1966). Obviously, grain size, which is also affected by crushability, as well as the shape of the grains, affect liquefaction potential (Rui et al., 2020). However, in our analysis, crushability favoring compressibility seems to prevail, thereby increasing the potential for liquefaction.

Marine carbonate sediments favor grain crushability, which leads to long-term mechanical degradation and affects liquefaction resistance. Thus, relying on existing literature for geotechncial design is risky, and basic lab analysis is crucial to understanding sediment behavior under cyclic and dynamic loads. Determining the CRR-particle crushability relationship (Figure 12) is particularly important.

It is important to note that our study refers to specific carbonate sediments, which are produced and accumulated in marine settings. Two main sources of sediments are identified (Sultan et al., 2023): (1) coarse carbonate sediments produced by the Mayotte barrier reef and exported offshore towards the adjacent slope, notably by turbidity currents, and (2) hemipelagic sediments (vulnerable to liquefaction according to our results) derived from the settling of dead foraminifer through the water column down to seafloor, possibly forming cm to m-thick sediment layers over time. Unlike low-liquefaction carbonate sands in coastal areas (e.g., LaVielle, 2008), carbonate sediments dominated by planktic foraminifer are found in distal settings, from the upper continental slope (150–200 m depth) to the abyssal plain.

Conclusions

In the present work, we explored the hypothesis that biogenic particles naturally deposited in offshore environments can break upon static or cyclic loading. We selected 38 samples from cores recovered from Mayotte’s slopes for further studies, of which 12 were tested for crushability in K_0 conditions discriminated by origin (carbonate- and volcanic-dominant). Then we tested 18 liquefied samples for crushability. Below are the most prominent conclusions of this study:

- Biogenic particles in naturally sedimented environments can crush upon external loading either in K_0 or cyclic conditions, while particles sizes > 10 microns seem to be the most impacted. Liquefaction resistance decreases with the increase in carbonate particles.
- Crushability of biogenic particles is likely to be the reason for failure in liquefaction-prone layers in Mayotte's slopes.
- It was established that in the case of Mayotte slope sediments, the loading threshold in K_0 condition was 500 kPa of effective stress.
- Recovered samples classify as SC-MH/OH or SM-MH/OH (sandy silt) with a bimodal distribution curve and D_{50} spanning from 22.8 to 129 μm. SEM images show large biogenic particles with internal porosity. Characterization results plot off-trend with respect to worldwide databases of sandy silts probably due to the higher water intake with respect to quarzitic soils. Therefore, standard characterization tests are biased and should not be used to describe these sediments and typical correlations cannot be implemented.
- Engineering properties fall off-trend from generally accepted values for sandy silt soils. Properties that vary with stress, such as compressibility, consolidation, and hydraulic conductivity, are further influenced by particle breakage.
- Samples with high fines content were susceptible to liquefaction highlighting the high complexity of this process.
- It is recommended to conduct laboratory tests to determine the relationship between CRR and particle crushability in order to conclude on its impact on wind farm design and other underwater infrastructure engineering.

Our results do not follow general trends found in the literature. We hypothesize that naturally sedimented soils lose structure and particle crushability, both of which contribute to liquefaction. We believe that the best way to test our hypothesis is to repeat the liquefaction tests: (1) within a μ-CT scanner to capture images of particle crushing under cyclic loading as a precursor of liquefaction failure; and (2) via DEM modeling to simulate an assembly of weak biogenic particles with varying sizes and shapes to determine local force concentrations and contact number evolution upon particle breakage.

Acknowledgments: Since June 2019, Mayotte seismo-volcanic activity is monitored by REVOSIMA (Réseau de surveillance volcanologique et sismologique de Mayotte - DOI: 10.18715/MAYOTTE.REVOSIMA) and funded by the Ministry for Ecological Transition and Territorial Cohesion (MTECT), the Ministry of Higher Education and Research (MESR), the Ministry of the Interior and Overseas (MIOM), with the support of the French Ministry for Armed Forces (MINARM). Marine operations benefit from the support of the French Oceanographic Fleet (FOF). Data compiled in this article was obtained during the cruise MAYOBS19. We thank the cruise scientific team, captains, crews and the chief scientists (E. Rinnert, E. Lebas and F. Paquet). Additionally, we appreciate the help from N. Bauchet (geotech characterization and lab testing), N. Tanguy (bathymetry visualization), N. Gayet (SEM images), M. Rovere, A. Roubi and J. Gouriou (grain-size analysis and lab quality control).

Notation

MSCL	Multi-Sensor Core Logger
γ-density	Gamma density
MS	Magnetic susceptibility
Gs	Specific gravity
D_{50}	Mean particle size

Cu	Coefficient of uniformity
FC	Fines content
LL	Liquid limit
PL	Plastic limit
PI	Plasticity index
Ss	Specific surface
w	Natural water content
e	Void ratio
e_o	In-situ void ratio
e_{1kPa}	Void ratio at σ’ = 1kPa
σ’	Effective stress
Cv	Primary consolidation coefficient
Cα	Secondary consolidation coefficient
Cc	Compressibility index
Cs	Swelling index
K_0	No lateral deformation loading conditions
k_{hyd}	Hydraulic conductivity
k_{ini}	Hydraulic conductivity at a reference void ratio ($e/e_0 = 1$)
δ-exponent	Hydraulic conductivity sensitivity parameter
ΔArea	Particle crushability
A_{post}	Post-test area below the grain-size cumulative curves
A_{und}	Undisturbed area below the grain-size cumulative curves
N	Cycle number
CRR	Cyclic resistance ratio
C	Lithology-dependent normalization factor

References

Andrews, D.C. and Martin, G.R., 2000, January. Criteria for liquefaction of silty soils. In Proc., 12th World Conf. on Earthquake Engineering (pp. 1-8).

ASTM, 2006. Standard test methods for specific gravity of soil solids by water pycnometer. ASTM international.

ASTM, 2011a. Standard Practice for Classification of Soils for Engineering Purposes (Unified Soil Classification System) 1. ASTM international.

ASTM, 2011b. Standard test methods for on-dimensional consolidation properties of soils using incremental loading. ASTM D2435/D2435M-11, West Conshohocken, PA.

ASTM, 2015. Standard test method for measurement of hydraulic conductivity of porous material using a rigid-wall, compaction-mold permeameter. ASTM D5856-15, West Conshohocken, PA.

ASTM, 2017. Standard test methods for liquid limit, plastic limit, and plasticity index of soils. ASTM D4318. West Conshohocken, PA.

Audru, J.C., Guennoc, P., Thinon, I. and Abellard, O., 2006. Bathymay: la structure sous-marine de Mayotte révélée par l'imagerie multifaisceaux. Comptes Rendus Geoscience, 338(16), pp.1240-1249.

Bachus, R.C., Terzariol, M., Pasten, C., Chong, S.H., Dai, S., Cha, M.S., Kim, S., Jang, J., Papadopoulos, E., Roshankhah, S. and Lei, L., 2019. Characterization and engineering properties of dry and ponded class-F fly ash. Journal of Geotechnical and Geoenvironmental Engineering, 145(3), p.04019003.

Beemer, R.D., Sadekov, A., Lebrec, U., Shaw, J., Bandini-Maeder, A. and Cassidy, M.J., 2019, March. Impact of biology on particle crushing in offshore calcareous sediments. In Eighth International Conference on Case Histories in Geotechnical Engineering (pp. 640-650). Reston, VA: American Society of Civil Engineers.

Boulanger, R.W. and Idriss, I.M., 2004. Evaluating the potential for liquefaction or cyclic failure of silts and clays (p. 131). Davis, California: Center for Geotechnical Modeling.

Boulanger RW, and Idriss IM, 2006. Liquefaction susceptibility criteria for silts and clays. J Geotech Geoenviron Eng ASCE 132(11):1413–1426

Brandes, H.G., 2011. Simple shear behavior of calcareous and quartz sands. Geotechnical and Geological Engineering, 29, pp.113-126.

Bray, J.D. and Sancio, R.B., 2006. Assessment of the liquefaction susceptibility of fine-grained soils. Journal of geotechnical and geoenvironmental engineering, 132(9), pp.1165-1177.

BS British Standards, 1990. Soils for civil engineering purposes. Part 2: Classification tests. BS 1377-2. London: BS.

Cesca, S., Letort, J., Razafindrakoto, H.N., Heimann, S., Rivalta, E., Isken, M.P., Nikkhoo, M., Passarelli, L., Petersen, G.M., Cotton, F. and Dahm, T., 2020. Drainage of a deep magma reservoir near Mayotte inferred from seismicity and deformation. Nature geoscience, 13(1), pp.87-93.

Coop, M.R., 1990. The mechanics of uncemented carbonate sands. Geotechnique 40, 607–626. .

Coop, M.R., Sorensen, K.K., Freitas, T.B., Georgoutsos, G., 2004. Particle breakage during shearing of a carbonate sand. Geotechnique 54, 157–164. https://doi.org/10.1680/geot.2004.54.3.157.

Courgeon, S., Bachèlery, P., Jouet, G., Jorry, S.J., Bou, E., BouDagher-Fadel, M.K., Révillon, S., Camoin, G. and Poli, E., 2018. The offshore east African rift system: new insights from the Sakalaves seamounts (Davie Ridge, SW Indian Ocean). Terra Nova, 30(5), pp.380-388.

Daniel, J., Dupont, J. and Jouannic, C., 1972. Relations Madagascar-archipel des Comores (Nord-Est du canal de Mozambique): sur la nature volcanique du Banc du Leven.

Deville, E., Marsset, T., Courgeon, S., Jatiault, R., Ponte, J.P., Thereau, E., Jouet, G., Jorry, S.J. and Droz, L., 2018. Active fault system across the oceanic lithosphere of the Mozambique Channel: Implications for the Nubia–Somalia southern plate boundary. Earth and Planetary Science Letters, 502, pp.210-220.

Daouadji, A., Hicher, P.Y., Rahma, A., 2001. An elastoplastic model for granular materials taking into account grain breakage. European Journal of Mechanics a-Solids 20, 113-137.

Einav I, 2007. Breakage mechanics—part I: theory. J Mech Phys Solids 55(6):1274–1297

Emerick, C.M. and Duncan, R.A., 1982. Age progressive volcanism in the Comores Archipelago, western Indian Ocean and implications for Somali plate tectonics. Earth and Planetary Science Letters, 60(3), pp.415-428.

Famin, V., Michon, L. and Bourhane, A., 2020. The Comoros archipelago: a right-lateral transform boundary between the Somalia and Lwandle plates. Tectonophysics, 789, p.228539.

Farrar, D.M. and Coleman, J.D., 1967. The correlation of surface area with other properties of nineteen British clay soils. Journal of Soil Science, 18(1), pp.118-124.

Feuillet, N., Jorry, S., Crawford, W.C., Deplus, C., Thinon, I., Jacques, E., Saurel, J.M., Lemoine, A., Paquet, F., Satriano, C. and Aiken, C., 2021. Birth of a large volcanic edifice offshore Mayotte via lithosphere-scale dyke intrusion. Nature Geoscience, 14(10), pp.787-795.

Franke, D., Jokat, W., Ladage, S., Stollhofen, H., Klimke, J., Lutz, R., Mahanjane, E.S., Ehrhardt, A. and Schreckenberger, B., 2015. The offshore East African Rift System: Structural framework at the toe of a juvenile rift. Tectonics, 34(10), pp.2086-2104.

Ghani, S. and Kumari, S., 2021. Insight into the effect of fine content on liquefaction behavior of soil. Geotechnical and Geological Engineering, 39, pp.1-12.

Gratchev I, Sassa K, and Fukuoka H, 2006. How reliable is the plasticity index for estimating the liquefaction potential of clayey sands? J Geotech Geoenviron Eng. 132(1):124–127

Hyodd, M., Hyde, A.F.L., Aramaki, N., 1998. Liquefaction of crushable soils. Geotechnique 48, 527-543.

Hyodo, M., Nakata, Y., Aramaki, N., Hyde, A.F. and Inoue, S., 2000, January. Liquefaction and particle crushing of soil. In Proc., 12th World Conf. on Earthquake Engineering.

Ishihara K, and Koseki J, 1989. Cyclic shear strength of fines-containing sands, Earthquake and Geotech. Engg. Japanese Society of Soil Mechanics and Foundation Engineering, Tokyo, pp 101–106

Ishihara, K., 1993. Liquefaction and flow failure during earthquakes. Geotechnique, 43(3), pp.351-451.

Jang, J., & Carlos Santamarina, J, 2017. Closure to "Fines classification based on sensitivity to pore-fluid chemistry by Jungbong Jang and J. Carlos Santamarina". Journal of Geotechnical and Geoenvironmental Engineering, 143(7), 07017013.

Kusky, T.M., Toraman, E., Raharimahefa, T. and Rasoazanamparany, C., 2010. Active tectonics of the Alaotra–Ankay Graben System, Madagascar: possible extension of Somalian–African diffusive plate boundary?. Gondwana Research, 18(2-3), pp.274-294.

LaVielle, T.H., 2008. Liquefaction susceptibility of uncemented calcareous sands from Puerto Rico by cyclic triaxial testing. MSc thesis, Virginia Tech.

Lee, C.Y., and Poulos, H.G., 1991. Tests on model instrumented grouted piles in offshore calcareous soil. Journal of geotechnical engineering 117, 1738-1753.

Marto, A., Tan, C.S., Makhtar, A.M., Ung, S.W. and Lim, M.Y., 2015. Effect of plasticity on liquefaction susceptibility of sand-fines mixtures. Applied mechanics and materials, 773, pp.1407-1411.

Mesri, G., 1973. Coefficient of secondary compression. Journal of the soil mechanics and foundations division, 99(1), pp.123-137.

Michon, L., 2016. The volcanism of the Comoros archipelago integrated at a regional scale. Active Volcanoes of the Southwest Indian Ocean: Piton de la Fournaise and Karthala, pp.333-344.

Mohtashami, E., Olgun, C.G., Wu, C. and Selly, T., 2023. Internal Structure and Breakage Behavior of Biogenic Carbonate Sand Grains. In Geo-Congress 2023 (pp. 565-574).

Murff, J.D., 1987. Pile capacity in calcareous sands: State if the art. Journal of Geotechnical Engineering 113, 490-507.

Nauroy, J.F. and LeTirant, P., 1985, May. Driven piles and drilled and grouted piles in calcareous sands. In Offshore Technology Conference (pp. OTC-4850). OTC.

Nougier, J., Cantagrel, J.M. and Karche, J.P., 1986. The Comores archipelago in the western Indian Ocean: volcanology, geochronology and geodynamic setting. Journal of African Earth Sciences (1983), 5(2), pp.135-145.

O’Connor, J.M., Jokat, W., Regelous, M., Kuiper, K.F., Miggins, D.P. and Koppers, A.A., 2019. Superplume mantle tracked isotopically the length of Africa from the Indian Ocean to the Red Sea. Nature communications, 10(1), p.5493.

Park, S.S. and Kim, Y.S., 2013. Liquefaction resistance of sands containing plastic fines with different plasticity. Journal of geotechnical and geoenvironmental engineering, 139(5), pp.825-830.

Polito C, 2001. Plasticity based liquefaction criteria. In: Proc. of the 4th intl. Conf. on recent advances in geotechnical earthquake engineering and soil dynamics.

Poulain, P., Le Friant, A., Pedreros, R., Mangeney, A., Filippini, A.G., Grandjean, G., Lemoine, A., Fernández-Nieto, E.D., Díaz, M.J.C. and Peruzzetto, M., 2022. Numerical simulation of submarine landslides and generated tsunamis: application to the on-going Mayotte seismo-volcanic crisis. Comptes Rendus. Géoscience, 354(S2), pp.361-390.

Prakash S, and Sandoval JA, 1992. Liquefaction of low plasticity silts. J Soil Dynamics and Earthquake Engg 71(7):373–397

Ren, X. W., and J. C. Santamarina. 2018. The hydraulic conductivity of sediments: A pore size perspective. Eng. Geol. 233: 48–54. https://doi .org/10.1016/j.enggeo.2017.11.022.

Rinnert, E., Lebas, E., Paquet, F., Jorry, S., Feuillet, N., Thinon, I., Fouquet, Y. 2019, MAYOBS, https://doi.org/10.18142/291.

Rui, S., Guo, Z., Si, T., and Li, Y., 2020. Effect of particle shape on the liquefaction resistance of calcareous sands. Soil Dynamics and Earthquake Engineering 137, 106302.

Salva Ramirez, M., and Santamarina, J. C., 2021. Specific Surface Area by Colorimetry and Image Analysis. Geotechnical Testing Journal, 45(1).

Sandoval, E.A., and Pando, M.A., 2012. Experimental assessment of the liquefaction resistance of calcareous biogenous sands. Earth Sciences Research Journal 16, 55-63.

Santamarina, J.C., Klein, A. and Fam, M.A., 2001. Soils and waves: Particulate materials behavior, characterization and process monitoring. Journal of Soils and Sediments, 1(2), pp.130-130.

Santamarina, J.C., Klein, K.A., Wang, Y.H. and Prencke, E., 2002. Specific surface: determination and relevance. Canadian Geotechnical Journal, 39(1), pp.233-241.

Seed, H.B., and Lee, K.L., 1966. Liquefaction of saturated sands during cyclic loading. Journal of the Soil Mechanics and Foundations Division 92, 105-134.

Seed HB, and Idriss IM, 1982. Ground motions and soil liquefaction during earthquakes. Earthquake Engineering Research Institute, Berkeley, Calif.

Seed, R.B., Cetin, K.O. and Moss, R.E.S., 2001, August. Recent advances in soil liquefaction hazard assessment. In 15th international conference on soil mechanics and geotechnical engineering, TC4 satellite conference on" Lessons learned from recent strong earthquakes.

Seed, R.B., Cetin, K.O., Moss, R.E., Kammerer, A.M., Wu, J., Pestana, J.M., Riemer, M.F., Sancio, R.B., Bray, J.D., Kayen, R.E. and Faris, A., 2003. Recent advances in soil liquefaction engineering: a unified and consistent framework. In Proceedings of the 26th Annual ASCE Los Angeles Geotechnical Spring Seminar: Long Beach, CA.

Shahnazari, H., Jafarian, Y., Tutunchian, M.A. and Rezvani, R., 2016. Probabilistic assessment of liquefaction occurrence in calcareous fill materials of Kawaihae Harbor, Hawaii. International Journal of Geomechanics, 16(6), p.05016001.

Sultan, N., Jouet, G., Riboulot, V., Terzariol, M., Garziglia, S., Cattaneo, A., Giraudeau, J. and Jorry, S.J., 2023. Sea-level fluctuations control the distribution of highly liquefaction-prone layers on volcanic-carbonate slopes. Geology, 51(4), pp.402-407.

Taylor, M. and Green, R.A., 2021, May. Simplified liquefaction triggering assessment of coral-derived carbonate sands. In Proceedings of the 20th international conference on soil mechanics and geotechnical engineering, Sydney, NSW, Australia (pp. 1-5).

Tong, C.X., Zhai, M.Y., Li, H.C., Zhang, S. and Sheng, D., 2022. Particle breakage of granular soils: changing critical state line and constitutive modelling. Acta Geotechnica, pp.1-14.

Tzevahirtzian, A., Zaragosi, S., Bachèlery, P., Biscara, L. and Marchès, E., 2021. Submarine morphology of the Comoros volcanic archipelago. Marine Geology, 432, p.106383.

Youd, T.L., 1998. Screening guide for rapid assessment of liquefaction hazard at highway bridge sites (No. MCEER-98-0005). Multidisciplinary Center for Earthquake Engineering Research (US).

Yu, F., 2019. Influence of particle breakage on behavior of coral sands in triaxial tests. International Journal of Geomechanics, 19(12), p.04019131.

Wang, W., 1979. Some findings in soil liquefaction. Earthquake Engineering Department, Water Conservancy and Hydroelectric Power Scientific Research Institute.

Wang, X., Cui, J., Zhu, C.Q., Wu, Y. and Wang, X.Z., 2021. Experimental study of the mechanical behavior of calcareous sand under repeated loading-unloading. Bulletin of Engineering Geology and the Environment, 80, pp.3097-3113.

Wetzel, A., 1990. Interrelationships between porosity and other geotechnical properties of slowly deposited, fine-grained marine surface sediments. Marine Geology, 92(1-2), pp.105-113.

Wiles, E., Watkeys, M. and Jokat, W., 2020. Surface expression of microplate boundary kinematics: an isolated abyssal hill in the Mozambique channel. Journal of African Earth Sciences, 168, p.103830.

Wu, Y., Li, N., Wang, X., Cui, J., Chen, Y., Wu, Y. and Yamamoto, H., 2021. Experimental investigation on mechanical behavior and particle crushing of calcareous sand retrieved from South China Sea. Engineering Geology, 280, p.105932.